JOURNAL OF GEOPHYSICAL RESEARCH, VOL. 100, NO. A6, PAGES 9669-9681, JUNE 1, 1995

Nonsteady state ionosphere-plasmasphere coupling of superthermal electrons

G. V. Khazanov and M. W. Liemohn

Space Physics Research Laboratory, Department of Atmospheric, Oceanic, and Space Sciences
University of Michigan, Ann Arbor

Abstract. Numerical solutions to the nonsteady state kinetic equation which describes the transport of superthermal electrons in the ionosphere and plasmasphere between the magnetically conjugate regions of the ionosphere are presented. The distribution function in time, distance along arbitrary geomagnetic field lines, energy, and pitch angle are among the parameters calculated by the model. This model represents a unified approach by self-consistently coupling the interaction of the two hemispheres and the trapping of superthermal electrons in the plasmasphere. Our calculations take into account the various ionization and excitation processes and the effect of an inhomogeneous magnetic field (i.e., magnetic mirroring of precipitating electrons and focusing of escaping electrons along magnetic field lines). Omnidirectional flux spectra and pitch angle distributions are shown for various L shells and situations, and the features are described in detail. Nonsteady state calculations predict that a depleted flux tube can take several hours to reach steady state levels again. Plasmaspheric transparencies are calculated for different conditions of illumination, scattering processes in the conjugate ionospheres, and field-aligned gradients of the thermal plasma density. Plasmaspheric transparency is found to be a complicated function of not only the plasmaspheric thermal plasma but also the ionospheric sources and scattering processes. A phenomenological model is used to describe the energy transmission, reflection, and deposition in the plasmasphere. By studying the ionosphere and plasmasphere as one system rather than two separate ones, substantial corrections are introduced in the values of key parameters describing photoelectron fluxes.

1. Introduction

A distinctive feature of the ionospheric plasma is a presence of superthermal electrons in the energy range of 1 to 500 eV. The superthermal electron population is formed due to ionization of neutral atmospheric atoms and molecules by photoionization (photoelectrons) or by impact ionization from energetic particles of magnetospheric origin (secondary electrons). Superthermal electrons play a very important role in a large number of ionospheric and plasmaspheric processes. A fairly detailed knowledge of the superthermal electron distribution function is required when modeling upper atmospheric phenomena, such as the heating of thermal plasma, optical emissions, ionization processes, plasma instabilities, or plasma wave generation.

Several methods have been used to calculate superthermal electron fluxes in the ionosphere (the differential flux is easily related to the distribution function). The simplest approach is a local equilibrium approximation [e.g., *Victor et al.*, 1976], in which the photoelectron flux is determined by balancing local production and loss mechanisms. This approximation is only valid at altitudes which are sufficiently low for transport effects to be neglected. For altitudes above 250 km, a more sophisticated approach must be applied which can account for the electron transport as well as for the interaction of electrons with other constituents. Over the last few decades many models have been developed to describe photoelectron transport and energy degradation processes (nonelastic collisions) of photoelectrons [cf. *Banks and Nagy*, 1970; *Mantas*, 1975; *Oran and Strickland*, 1978; *Prather et al.*, 1978; *Lejeune*, 1979; *Torr et al.*, 1990; *Link*, 1992; *Khazanov et al.*, 1992] as well as the transport of auroral (secondary) electrons [*Banks et al.*, 1974; *Mantas and Walker*, 1976; *Strickland et al.*, 1976; *Khazanov*, 1979; *Stamnes*, 1980; *Gefan et al.*, 1985; *Porter et al.*, 1987; *Lummerzheim et al.*, 1989]. Except for *Khazanov* [1979] and *Torr et al.* [1990], these calculations were based on the separate treatments of superthermal electrons in the ionosphere and in the plasmasphere (for a comprehensive review see *Khazanov et al.* [1994]).

Khazanov and Gefan [1982] and *Khazanov et al.* [1994] developed a comprehensive model which is equally valid in the ionosphere and in the plasmasphere and self-consistently couples the two hemispheres. *Khazanov et al.* [1994] have also shown that this self-consistent approach produces significant changes in the superthermal electron distributions compared to "pure" ionospheric or plasmaspheric calculations.

Among the numerous papers devoted to the superthermal electron transport between the magnetoconjugate regions of the ionosphere, no results have yet been published which describe the evolution and formation of superthermal electron fluxes under nonstationary conditions. Such models may be needed when the local source of superthermal electrons increases or decreases rather sharply, such as during sunrise and sunset, auroral precipitation events, or plasmaspheric refilling. During these short periods, strongly anisotropic distributions of superthermal electrons are generated, which may be sources of plasma instabilities and anomalous heating of the thermal plasma.

Paper number 95JA00526.
0148-0227/95/95JA-00526$05.00

Gefan and Khazanov [1990] have demonstrated the ability to model the time-dependent behavior of superthermal electrons. They simplified the problem by bounce-averaging the trapped population, and the time constants for filling the trapped region were found. The time to reach steady state for filling a flux tube with superthermal electrons was found to be shorter than, or of the order of, the time constant of the source for sunrise conditions. However, it was also shown that for the case when the flux tubes are depleted of thermal plasma, as after a magnetic storm, the time constants associated with the refilling may be considerably longer, thus meriting a time-dependent description of the problem. Recently, *Khazanov et al.* [1993a] have made the next step and considered the nonsteady state superthermal electron transport in the plasmasphere (at altitudes greater than about 1000 km) on the basis of kinetic equation in the guiding center approximation.

In this paper the first results of a numerical study of the nonsteady state ionosphere-plasmasphere coupling are presented. This new model is based on the generalization of the numerical codes by *Khazanov et al.* [1993a, 1994].

2. Mathematical Formulation

The kinetic equation includes the effects of elastic and inelastic collisions with both neutral and charged particles, transport in the inhomogeneous geomagnetic field, and particle sources can be written as [*Khazanov et al.*, 1993a, b]

$$\frac{\beta}{\sqrt{E}}\frac{\partial\phi}{\partial t}+\mu\frac{\partial\phi}{\partial s}-\frac{1-\mu^2}{2}\frac{1}{B}\frac{\partial B}{\partial s}\frac{\partial\phi}{\partial\mu}= Q+S_{ee}+\sum_i S_{ei}^0+\sum_\alpha S_{e\alpha}^0+\sum_\alpha S_{e\alpha}^*+\sum_\alpha S_{e\alpha}^+ \quad (1)$$

where $\beta=1.7\times10^{-8}$ $eV^{1/2}$ $cm^{-1}s$, $\phi=\phi(t, E, \mu, s)$ is the differential flux of electrons, μ is the pitch angle cosine, E is the energy, s is the coordinate parallel to the geomagnetic field B, and Q is the electron production rate due to photoionization of neutral particles. The collisions are given by S_{ee}, S_{ei}^0, $S_{e\alpha}^0$, $S_{e\alpha}^*$, and $S_{e\alpha}^+$ in (1) and represent the collision integrals of superthermal electrons with thermal electrons,

$$S_{ee}=An_e\left\{\frac{\partial}{\partial E}\left[\frac{\phi}{E}+T_e\frac{\partial}{\partial E}\left(\frac{\phi}{E}\right)\right]+\frac{1}{4E^2}\frac{\partial}{\partial\mu}\left[\left(1-\mu^2\right)\frac{\partial\phi}{\partial\mu}\right]\right\} \quad (2)$$

with thermal ions,

$$S_{ei}^0=An_i\left\{\frac{m}{m_i}\frac{\partial}{\partial E}\left[\frac{\phi}{E}+T_i\frac{\partial}{\partial E}\left(\frac{\phi}{E}\right)\right]+\frac{1}{4E^2}\frac{\partial}{\partial\mu}\left[\left(1-\mu^2\right)\frac{\partial\phi}{\partial\mu}\right]\right\} \quad (3)$$

elastic scattering with neutral particles,

$$S_{e\alpha}^0=2\frac{m}{m_\alpha}n_\alpha\frac{\partial}{\partial E}\left\{\sigma_\alpha^{(1)}E^2\left[\frac{\phi}{E}+T_n\frac{\partial}{\partial E}\left(\frac{\phi}{E}\right)\right]\right\}+n_\alpha\int I_\alpha(E,\chi)[\phi(E,\mu')-\phi(E,\mu)]d\Omega \quad (4)$$

inelastic excitation scattering with neutral particles,

$$S_{e\alpha}^*=n_\alpha\sum_j\left[\sigma_{\alpha j}^*\left(E+E_{\alpha j}^*\right)\phi\left(E+E_{\alpha j}^*,\mu\right)-\sigma_{\alpha j}^*(E)\phi(E,\mu)\right] \quad (5)$$

and inelastic ionization scattering with neutral particles,

$$S_{e\alpha}^+=n_\alpha\left\{\int_{E+E_\alpha^+}^{2E+E_\alpha^+}I_\alpha^+\left(E',E'-E-E_\alpha^+\right)\phi\left(E',\mu\right)dE'+\frac{1}{2\pi}\int_{2E+E_\alpha^+}^{\infty}I_\alpha^+\left(E',E\right)\left[\int_0^{2\pi}\phi\left(E',\sqrt{1-\mu^2}\cos\varepsilon\right)d\varepsilon\right]dE'-\sigma_\alpha^+(E)\phi(E,\mu)\right\} \quad (6)$$

from *Khazanov et al.* [1994]. Here $A=2\pi e^4 ln\Lambda = 2.6\times10^{-12}$ eV^2cm^2, where $ln\Lambda$ is the Coulomb logarithm, m is the electron mass, n_e, n_i, and n_α are the density of electrons, ions and neutral particles of species α, T_e, T_i, and T_n are the temperatures of electrons, ions and neutral particles of species, $\sigma_\alpha^{(1)}(E)=\int I_\alpha(E,\chi)(1-\cos\chi)d\Omega$ is the transport cross section, χ is the scattering angle, and $I_\alpha(E,\chi)$ the differential elastic cross section; $\sigma^*_{\alpha j}$ is the total cross section of scattering for bringing a neutral particle into an excited state characterized by a threshold energy $E^*_{\alpha j}$, E^+_α is the ionization energy, ε is the azimuthal scattering angle, and $\cos\theta' = \cos\chi\cos\theta + \sin\theta\sin\chi\cos\varepsilon$. We also have

$$\sigma_\alpha^+(E)=\int_0^{(E-E_\alpha^+)/2}I_\alpha^+(E,E_2)dE_2$$

which is the total cross section of ionization by an electron with an energy E, where $I_\alpha^+(E,E_2)$ is the appropriate differential cross section, and E_2 is the energy of a secondary electron.

Terms of order m/m_i and the second derivative with respect to energy will be omitted from the calculations [*Khazanov et al.*, 1994].

In order to decrease undesirable computational effects associated with approximation errors of the derivatives $\partial/\partial s$ and $\partial/\partial\mu$, it is convenient to change variables from (μ, s) to (μ_0, s) [*Khazanov et al.*, 1993a], where

$$\mu_0=\frac{\mu}{|\mu|}\sqrt{1-\frac{B_0}{B(s)}(1-\mu^2)} \quad (7)$$

with B_0 and μ_0 denoting the magnetic field and the cosine of the pitch angle at the magnetic equator of the flux tube. This change of variables is desirable because $\phi(\mu_0,s)$ now is a slowly varying function with s (μ_0 is the adiabatic invariant). The region over which $\phi(\mu_o,s)$ is defined in terms of s and μ_0 is shown in Figure 1 of *Khazanov et al.* [1993a]. The loss cone is defined by $\mu_{0b}\le|\mu_0|\le1$ and the trapping region by $(1-B_0/B(s))\le\mu_0^2\le\mu_{0b}^2$, where $\mu_{0b}^2=(1-B_0/B(s_1))$ is the loss cone boundary and $B(s_1)$ is the magnetic field at the low altitude boundary. The reflection point is determined from the condition $\mu=0$: $B(s_{ref})=B_0/(1-\mu_0^2)$.

Using the numerical technique developed by *Khazanov* [1979], (1) has been solved for these new variables (t, E, $\mu_0(\mu,s)$, s) under the following boundary conditions:

$$\phi(t=0,s,\mu_0,E)=\Psi_0(s,\mu_0,E) \quad (8)$$

$$\phi(t, s=-s_1, \mu_0, E) = \Psi^-(t, \mu_0, E); \quad -1 \le \mu_0 \le -\sqrt{1-B_0/B(-s_1)}$$
$$\phi(t, s=s_1, \mu_0, E) = \Psi^+(t, \mu_0, E); \quad \sqrt{1-B_0/B(s_1)} \le \mu_0 \le 1 \tag{9}$$

$$\frac{\partial \phi(\theta_0 = 0, \pi)}{\partial \theta_0} = 0; \theta_0 = \cos^{-1}\mu_0 \tag{10a}$$

$$\phi^+(t, s, \mu_0 = \mu_{0_b}, E) = \phi^-(t, s, \mu_0 = -\mu_{0_b}, E) \tag{10b}$$

$$\frac{\partial \phi^+}{\partial \theta_0}(t, s, \mu_0 = \mu_{0_b}, E) = -\frac{\partial \phi^-}{\partial \theta_0}(t, s, \mu_0 = -\mu_{0_b}, E) \tag{10c}$$

$$\phi(t, s, \mu_0, E = 0; E = E_{max}) = 0 \tag{11}$$

where Ψ_0 is the initial distribution in the flux tube (in the refilling case, which will be discussed later, Ψ_0 is taken to be zero everywhere); $\Psi^{\pm}$ are the low altitude (in our case, 90 km) boundary fluxes which were calculated from (1) for the condition of local equilibrium; and θ_0 is the equatorial pitch angle. The structure of the kinetic equation (1) and its solution was discussed in great detail by *Khazanov et al.* [1993a, 1994].

To perform the calculations in this paper we used the following input for our superthermal electron model. Solar EUV and X-ray radiation spectra were obtained using the *Hinteregger* [1981] model, while neutral thermospheric densities and temperatures were given by MSIS-90 [*Hedin*, 1991]. The electron profile in the ionosphere was calculated based on the IRI model [*Bilitza*, 1990] and extended in the plasmasphere region using the assumption that the electron thermal density distribution in the plasmasphere is proportional to the geomagnetic field. To represent geomagnetically quiet times, we used the distribution $n_e \sim B$ which corresponds to a filled plasmasphere [*Newberry et al.*, 1989]. The case $n_e \sim B^2$ will indicate some intermediate step which will occur during plasmaspheric refilling [*Khazanov et al.*, 1984]. Photoabsorption and photoionization cross sections for O, O_2, and N_2 were taken from *Fennelly and Torr* [1992]. Partial photoionization cross sections for O_2 and N_2 were obtained from *Conway* [1988], while partial photoionization cross sections of *Bell and Stafford* [1992] were adopted for atomic oxygen. Cross sections for elastic collisions, state-specific excitation and ionization were taken from *Solomon et al.* [1988]. All of the calculations were performed for a local time of noon at equinox, with $F_{10.7}$ and $\langle F_{10.7} \rangle$ values of 150, chosen so the atmospheric conditions are symmetric and the solar radiation is at an average intensity level.

3. Results

The main objective of this paper is to demonstrate the capabilities of the nonsteady state ionosphere-plasmasphere superthermal electron transport model and to indicate the possibilities for future research now available. One feature is that the model does not assume anything about the macroscopic magnetic field. The model is capable of handling an arbitrary geometry for the geomagnetic field: open or closed field lines; dipole or a more complex description; tilting of the geomagnetic axis; or any other configuration. For the results shown here, a dipole magnetic field was oriented symmetrically about the equator. For most of the results, symmetric atmospheric illumination was used, meaning that the conjugate atmospheres had the same density profiles and photoelectron production rates. However, a few nonsymmetric atmospheres were used, where the only difference is that the photoelectron production rate is set to zero in one of the atmospheres (referred to as dark).

Another feature of the model is that it can handle an arbitrary grid with respect to energy, distance, or pitch angle to facilitate efficient computation. For our applications, the step sizes with respect to energy, distance, and pitch angle were determined through successive trials of the code. The energy grid will determine the resolution of the fine structure in the superthermal electron spectrum, such as the photoelectron source peaks in the 20-30 eV range due to He II-304 Å. An energy step of 1 eV was used for the present study. The range of energies calculated is from 1 to 150 eV, and the fluxes at energies above 150 eV were assumed to be zero. The spatial grid was determined by first choosing a starting grid so the steps are less than the local mean free paths, and then decreasing the step size until the solution no longer changed significantly. It was found that 34 grid points in each ionosphere is sufficient and does not need to be altered for different L shells. Because of the lengthening of the magnetic flux tube, however, the number of plasmaspheric steps increases with L shell, ranging from 90 points for L=2 up to 190 points for L=6. The pitch angle grid, like the spatial grid, has a variable step size. Since the flux does not change much through the loss cone, five to ten points is sufficient in this region for any L shell. In contrast, a large gradient exists in the transition region between the loss cone and the trapped zone which depends on L shell, and so the total pitch angle grid points in the equatorial trapped zone (0° to 180°) ranges from 200 for L=2 to 300 for L=6. The number of spatial and pitch angle grid points is the optimum number for this numerical technique; less points change the results and more points are unnecessary.

The time step was chosen to be less than the characteristic timescales of all the processes in (1). For example, in the collision-dominated region, the time step must be much less than the time between elastic collisions, and in the transport-dominated region, the time step must satisfy the Courant stability condition, $\Delta t \le \Delta s/v$, where v is the superthermal electron speed.

The numerical technique includes an iterative process due to the interplay between the upward and downward flowing particles at 90°. Thus, at each time step and each energy, the program iterates over the spatial and pitch angle calculations until the fluxes converge within a preset ratio to the previous iteration. This convergence factor is taken to be three percent in the present calculations.

Our numerical technique is similar to the techniques used by *Khazanov et al.* [1993a, 1994]. In order to check the validity of this numerical scheme, *Khazanov et al.* [1994] compared their results for "pure" plasmaspheric transport with analytical solutions by *Khazanov et al.* [1992] and Monte Carlo simulations by *Takahashi* [1973], and found good agreement in all cases. Also, in *Khazanov et al.* [1994], ionospheric comparisons showed good agreement with DE 2 data and other ionospheric models of superthermal electrons. Additionally, for the steady state calculation, we checked the energy conservation of our scheme, finding that the energy is conserved within the convergence criteria of three percent.

3.1. Steady State Results

It is useful to start our discussion with the case of steady state ionosphere-plasmasphere superthermal electron

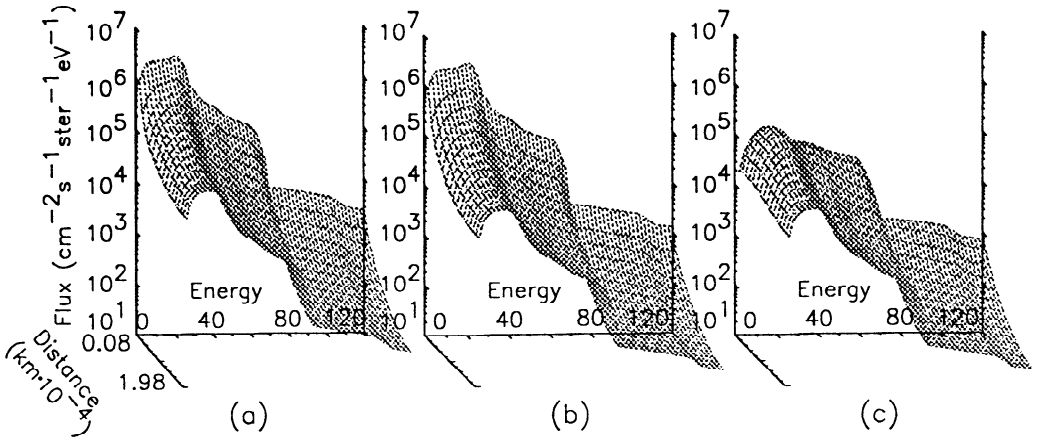

Figure 1. Steady state omnidirectional fluxes from the top of the ionosphere to the equatorial plane at L=3 with n_e~B, for (a) symmetric conditions of illumination and for nonsymmetric conditions for the (b) sunlit hemisphere and (c) the dark hemisphere.

coupling. The steady state solution was obtained by making the time step infinite, and tests concluded that this method of jumping to the steady state produces the same results as stepping slowly in time toward the convergent solution. Steady state results from the model for L=3 with the thermal density in the plasmasphere proportional to the magnetic field are shown in Figures 1 and 2. Figure 1a is the omnidirectional flux from the base of the plasmasphere (h=800 km) to the equator with symmetric conditions of illumination. The decrease at low energies is due to Coulomb collisions with the thermal plasma. The maximum in the spectrum near 20 eV is from the photoelectron source in that region, and the 20-30 eV range still contains some of the fine structure of the peaks due to the He II-304 Å resonance line. At several energies, the photoelectron production rate has a sharp decrease, and the spectrum shows these decreases in the 60-70 eV range and again near 110 eV. Except for these drops, the spectrum above 30 eV is smooth because there are no significant production peaks in this energy range and Coulomb collisions are slow because the cross section decreases proportional to E^{-2}. There are two reasons for the drop in omnidirectional flux toward the equator: Coulomb collisions are transferring energy to the thermal plasma and the magnetic flux tube cross sectional area increases.

Figures 1b and 1c show the energy spectrum for nonsymmetric illumination of an L=3 flux tube. Figure 1b shows omnidirectional fluxes from the sunlit ionosphere to the equatorial plane, and the other half of the plasmasphere, from the equator to the dark ionosphere, is shown in Figure 1c, so the curve at the equator (1.98 x 10^4 km) is the same for the two plots. These results demonstrate the difference in plasmaspheric flux depending on the ionospheric conditions; the fluxes near the sunlit atmospheres in Figures 1a and 1b have a similar energy spectrum, but the fluxes near the dark atmosphere in Figure 1c are lower than those in Figure 1a by almost an order of magnitude for low energies and by a factor of 2 for high energies (E>70 eV). For the energy grid used for these calculations, most of the structure in the 20-30 eV range due to the He II-304 Å resonance line has disappeared near the dark atmosphere. This occurs not only because there is no photoelectron source in the connected ionosphere but also because Coulomb collisions have smoothed the energy distribution as

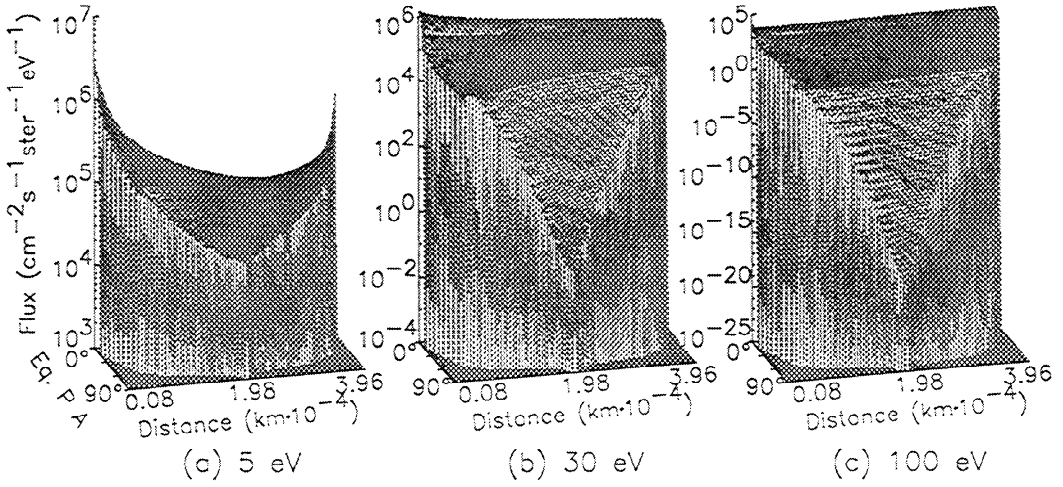

Figure 2. Steady state pitch angle distributions in the plasmasphere of upward flowing electrons for symmetric conditions of illumination at L=3 with ne~B for (a) 5 eV, (b) 30 eV, and (c) 100 eV.

the particles move through the plasmasphere from the sunlit hemisphere. The fine structure of these peaks would be more pronounced in the plasmaspheric spectrum if the energy resolution was higher. However, even for higher resolution grids, Coulomb collisions will still smooth away part of the fine structure. Since Coulomb collisions at this altitude are primarily with the thermal plasma, the amount of smoothing that the spectrum experiences through the plasmasphere may be an indication of the integral content of the flux tube.

Figure 2 contains a series of pitch angle distributions through the plasmasphere for an L=3 flux tube with symmetric conditions of illumination. The equatorial plane is located at the middle of each plot, with the two ionospheres connecting to each end of the plot. The distribution is plotted for equatorial pitch angles, and so the areas outside the region of existence of the solution (see Figure 1 of *Khazanov et al.* [1993a]) are shown as a flat surface at the bottom of the scale. Also, each plot is only half of the pitch angle distribution (0° to 90°), because the upward fluxes a given distance from its source ionosphere are identical to the downward fluxes that are the same distance from its source ionosphere. The loss cone region is located from 0° to 10°. The first surface Figure 2a shows 5 eV fluxes, the second surface Figure 2b shows 30 eV fluxes, and the third surface Figure 2c shows 100 eV fluxes.

The 5 eV particles, Figure 2a, are strongly influenced by Coulomb interactions with the thermal plasma. The distribution function has a drop of over an order of magnitude in the loss cone flux level from the ionosphere boundary to the equator because of Coulomb collisions, and the trapped zone shows an order of magnitude decrease from 10° to 90° at the equator due to Coulomb scattering. Notice that the 5 eV loss cone fluxes increase as the electrons approach the conjugate ionosphere. This increase is due to downward flowing electrons, streaming out of the conjugate ionosphere, backscattering into the upward flowing stream due to collisions with the thermal plasma.

In Figures 2b and 2c for 30 eV and 100 eV, respectively, Coulomb interactions are less effective because the cross section is proportional to E^{-2}, and this is seen in the loss cone and trapped zone fluxes in these two plots. The 30 eV surface plot shows a loss cone flux decrease of close to an order of magnitude through the entire plasmasphere, not after half of the plasmasphere as seen in the 5 eV fluxes of Figure 2a, and the 100 eV surface plot has a smaller drop in the loss cone, decreasing by a factor of 2 between the conjugate ionospheres. The trapped zones of Figures 2b and 2c show huge drops in flux, for 30 eV the drop is 7 orders of magnitude and 100 eV drops 20 orders of magnitude. Also notice that neither of these energies shows an increase in the flux as the particles move toward the conjugate ionosphere. This is because electrons at these higher energies backscatter very slowly and therefore the downward flowing electrons do not noticeably contribute to the upward streaming fluxes.

3.2. Nonsteady State Results

A nonsteady state calculation is needed to understand the superthermal electron behavior when the source changes rapidly, such as sunrise or sunset conditions, auroral precipitation events, artificial injection of energetic electrons from the spacecraft, or plasmaspheric refilling. During the refilling process, for instance, the streaming of electrons into the plasmasphere creates an electric field and couples the superthermal electrons to the ions. As the plasma flows up and out of the topside ionosphere, the flow conditions change from subsonic to supersonic, from collision-dominated to collisionless, and from O^+ dominance to H^+ dominance. In the collisionless regime, the ion velocity distributions become highly non-Maxwellian and the coupling between various plasma species occurs through the development of a self-consistent potential. Superthermal electrons, which form due to ionization of the atmosphere by solar radiation or by impacts from energetic particles of magnetospheric origin, can redistribute the self-consistent potential in the plasma. We expect that the presence of the enhanced high-velocity tail in the electron distribution will increase the number of fast ions. Because of enhanced ion acceleration in an expanding plasma, the initial superthermal electron distribution function may be changed. We also believe that only a nonsteady state superthermal electron transport model can properly handle the early stages of the plasmaspheric refilling process. We plan to couple our superthermal electron model with a transport model of the thermal plasma in the ionosphere and plasmasphere and to discuss the issue of the self-consistent potential formation in a forthcoming publication. For the purposes of this study, we excluded the electric field from (1) and assume that the thermal plasma density is quasi-neutral and constant with time.

Even without the electric field, numerical solutions of the kinetic equation given by (1) are technically very complicated because the characteristic timescales at various altitudes along the field line and for specific energies can be quite different. An important timescale to consider is the elastic scattering timescale, τ_c, because it is the fastest collisional timescale. This timescale depends on the elastic collision frequency and the particle speed, which are functions of energy. It also depends on the neutral atmosphere and thermal plasma densities, which are functions of position along the field line. Therefore τ_c is different for each energy and for each altitude. It can range from a tenth of a second to an hour (see Table 1). For instance, at L=2, 5 eV electrons can have an elastic scattering timescale of 0.1 s at 300 km, while the timescale for 100 eV electrons is 1200 s at the equatorial plane.

The huge spread of characteristic timescales makes it difficult to choose a time step that will treat each of these regions and energies appropriately. A time step of 0.01 s is appropriate for the lower ionosphere, but convergence in the plasmasphere would be very slow. A step of 10 s is appropriate for the plasmasphere, but then the ionospheric fluxes converge rapidly and the time-dependent features there cannot be seen. It is possible, however, to avoid this problem by switching to a dimensionless time t_D. This was done by dividing both sides of the kinetic (1) by the total scattering term, yielding the time-dependent transfer equation, similar to the approaches used by *Strickland et al.* [1976], *Oran and Strickland* [1978], and *Link*

Table 1. Elastic Collision Timescales for L=2

Altitude, km	E=5 eV	E=30 eV	E=100 eV
30	0.10	1.5	9.0
500	0.32	4.7	29
800	1.6	23	140
10,000 (eq.)	13	200	1200

[1992] (see, for example, *Strickland et al.* [1976, equation (2)]). The advantage is that times are compressed or expanded so the calculation is performed with the same dimensionless timescale for all altitudes and energies, while the drawback is that the results can become difficult to interpret because of the differences in real time equivalents for a given dimensionless time. Several tests were conducted to determine the correct time step for the calculations. It was also determined that the two methods (real time or dimensionless time) produce equivalent results for a given time.

To simulate the refilling process correctly, the proper initial and boundary conditions must be used. This includes not only superthermal electron conditions, but also the thermal plasma distribution. Unfortunately, these conditions are not yet definitively known. For the nonsteady state results presented here, the calculations begin with no superthermal electrons in the flux tube. There is experimental [*Carpenter and Park*, 1973; *Park et al.*, 1978; *Corcuff et al.*, 1972] and theoretical [*Khazanov et al.*, 1984] evidence that during geomagnetic disturbances, the equatorial thermal plasma can decrease to levels as low as 10^{-1} to 1 cm^{-3}. A nonsteady state thermal plasma transport model in the ionosphere and plasmasphere should be used to simulate this density decrease and the subsequent refilling, but the coupling of a thermal plasma model with our superthermal electron model is beyond the scope of this presentation and will be discussed in an upcoming publication. Nevertheless, there are several ways of modeling this plasmaspheric density decrease. One method is to use a different density distribution in the plasmasphere, such as $n_e \sim B^2$ rather than $n_e \sim B$. Another method would be to decrease the ionospheric densities by dividing the IRI model results by some factor, and thus reduce the plasmaspheric thermal density. Still another would be to use the IRI correction method proposed by *Buonsanto* [1989] to scale the topside ionosphere density down. *Buonsanto* [1989] showed that incoherent scatter radar observations of the thermal density in the ionosphere are lower than IRI densities at altitudes above the F_2 peak, and he provides a simple correction to the IRI model. *Kozyra et al.* [1990] uses this thinner F_2 layer model when calculating the solar cycle variations of stable auroral red arcs. By choosing the correct scaling factors, this method can be used to maintain the IRI model F_2 peak but decrease the density above this altitude to a target topside ionosphere density. Two of these methods will be demonstrated by results of this section.

The first results presented use the IRI densities in the ionosphere with the plasmaspheric densities proportional to the square of the magnetic field. Upward flowing fluxes are shown for 30 eV in Figure 3 for four altitudes (300 km (Figure 3a), 500 km (Figure 3b), 800 km (Figure 3c), and 10,000 km (Figure 3d)) along an L=2 field line. The first altitude is near the thermal electron density peak, the next altitude is in the transition region of the ionosphere, the third altitude is the top of the ionosphere, and the last altitude is at the equatorial plane in the plasmasphere. The dimensionless times presented are at t_D=0.1, 0.4, 0.7, 1.0, 2.0, and the steady state flux values. The equivalent real times for t_D=1.0 are presented in Table 1.

In Figure 3a, each time presented shows a uniform distribution because the elastic scattering with the thermal plasma and the neutral particles is very efficient. The fluxes in Figure 3b show a decrease at large pitch angles, especially in the steady state results. This is because of the path length to traverse a given field-aligned distance is longer for a large pitch angle electron compared to an electron with a smaller pitch angle, and so these longer-path particles undergo more collisions. This decrease at larger pitch angles is also seen at 800 km (Figure 3c), even at t_D=0.1. Once in the plasmasphere, however, the focusing of the electrons due to the changing magnetic field strength creates a maximum in the pitch angle distribution in the loss cone, which is 20° at the equator for L=2. Coulomb collisions with the thermal plasma scatters electrons into the trapped zone, though, and Figure 3d shows a gradual decrease with pitch angle of two orders of magnitude from the loss cone to 90°. Notice that the loss cone fluxes are continually decreasing, dropping by a factor of two from the F_2 peak to the equatorial plane.

It should be noted that for this thermal density distribution, none of the results at t_D=2.0 have reached the steady state results in Figure 3, indicating that another elastic scattering timescale or more is needed for convergence.

Time-dependent field-aligned omnidirectional flux spectra in the plasmasphere are shown in Figure 4. These calculations

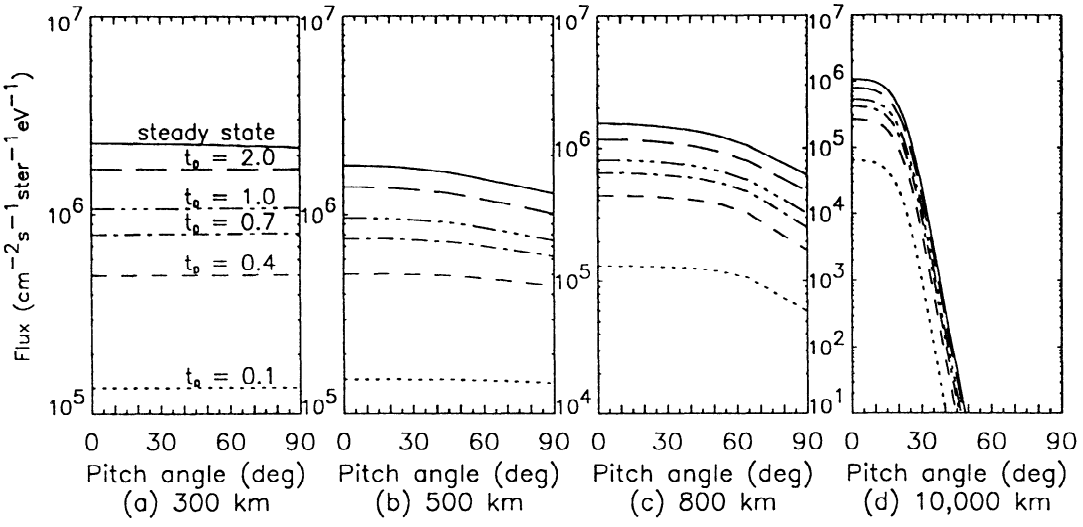

Figure 3. The 30 eV upward flowing pitch angle distributions for L=2 with $n_e \sim B^2$, with dimensionless times given in the figure and real time equivalents given in Table 1.

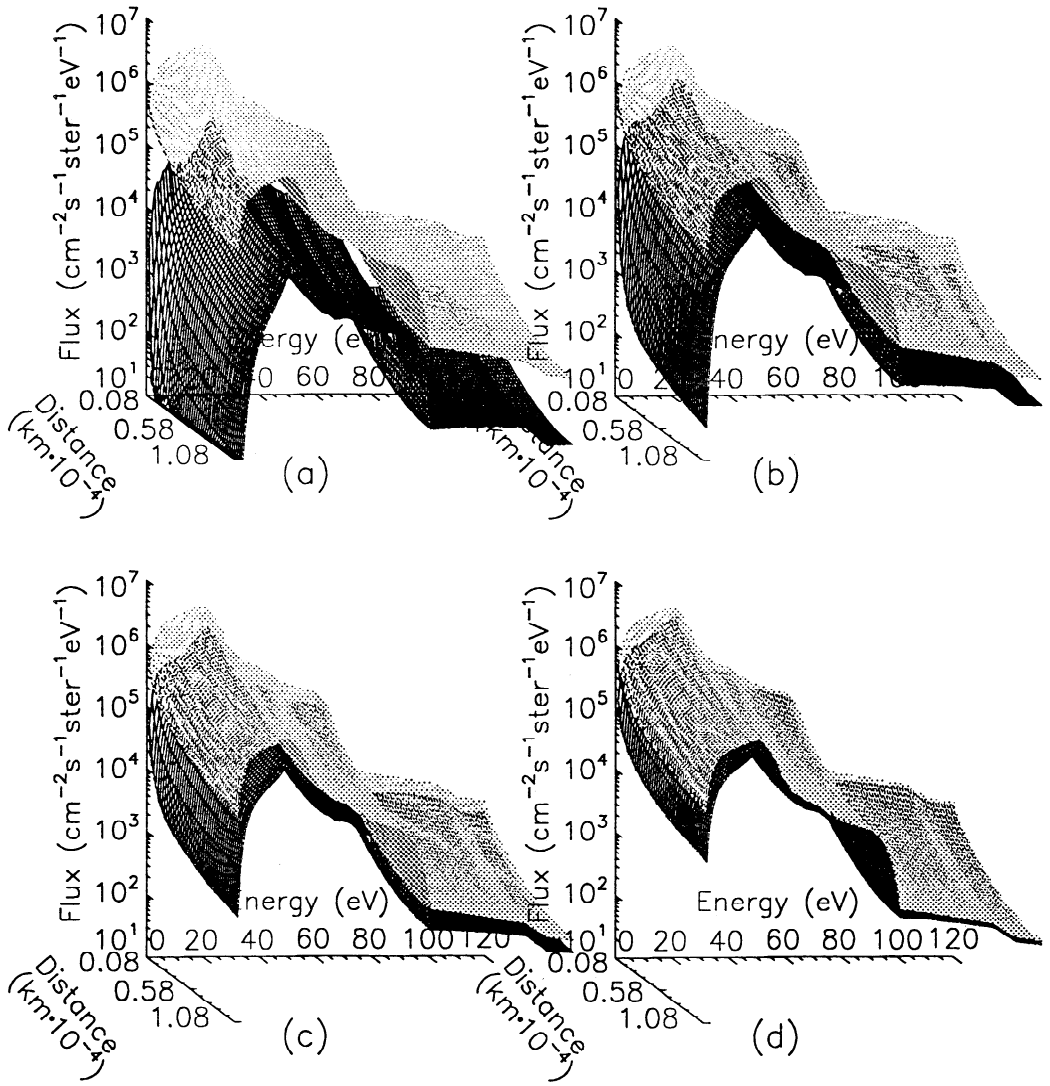

Figure 4. Omnidirectional fluxes for L=2 with n_e~B^2 from the top of the ionosphere to the equatorial plane at (a) t_D=0.1, (b) t_D=0.5, (c) t_D=1.0, and (d) t_D=2.0 with the steady state spectrum lightly superimposed on each plot.

also used the IRI densities in the ionosphere with n_e~B^2 in the plasmasphere. The nonsteady state fluxes presented for the dimensionless times t_D=0.1 Figure 4a, 0.5 Figure 4b, 1.0 Figure 4c, and 2.0 Figure 4d, with the steady state spectrum also plotted lightly on each of the figures so the progression of the solution can be seen more clearly. Note that for a given dimensionless time each grid point corresponds to a different real time due to the energy and spatial dependence of τ_c, and so even though it appears that the lower energies are taking longer to reach steady state, their real times are actually smaller than the high-energy times. The smaller flux values at low energies is due to the increased effect of Coulomb collisions as energy decreases. As the solution develops, these lower-energy fluxes increase not only due to the ionospheric source of particles, but also from the cascading of electrons from higher energies. The peaks in the 20 to 30 eV range are due to photoionization by the He II-304 Å resonance line. The differences in energy thresholds for the ionization states of the neutral species creates a range of structure in the photoelectron spectrum. Notice that the first few time steps show more of the fine structure than the steady state results. This is because Coulomb collisions smooth the distribution, and this smoothing continues with time. The energy grid will also determine the resolution of the fine structure of the spectrum. The sharp drop in the flux around 70 eV, as discussed before, is due to a corresponding decrease in the primary photoelectron spectrum. Because the t_D=2.0 fluxes are not at the steady state levels yet, as was the case in Figure 3, a dimensionless time calculation must be conducted for perhaps three or more characteristic elastic scattering timescales to reach the steady state solution. This means the fluxes in the trapped zone require several elastic collisions before the trapped zone is filled.

Using a different method to achieve a depleted thermal plasma density distribution, the IRI model was decreased above the F_2 peak following the *Buonsanto* [1989] method with different scaling factors to make the thermal plasma density at the topside ionosphere 545 cm^{-3}, and then n_e~B was used in the plasmasphere with L=3. This brings the equatorial thermal plasma density down to 17 cm^{-3}, which is still within the depleted density range [*Carpenter and Park*, 1973; *Park et al.*, 1978; *Corcuff et al.*, 1972; *Khazanov et al.*, 1984]. This is also the same distribution used in Figure 3 of *Khazanov et al.*

[1993a], where the refilling process was modeled using a plasmaspheric transport model with boundary conditions at 1000 km. Figures 5a and 5b show normalized equatorial pitch angle distributions from this calculation for 5 eV and 30 eV, respectively. This was a dimensional time calculation conducted for one hour of refilling. The steady state equatorial distributions that these results were normalized to are given in Figure 5c. Note that the steady state distributions continue below the presented flux range. Notice that the loss cone fluxes reach steady state in less than a minute. For this greatly depleted case, however, the 5 eV trapped zone fluxes take more than 30 min to reach steady state and the 30 eV fluxes are still far from the convergent levels after an hour of refilling. Therefore, the superthermal electron plasmaspheric refilling process could take hours and a time-dependent model must be used. Also, the low energy flux levels are dependent on the high-energy fluxes because of the energy cascading due to Coulomb collisions, so the 5 eV fluxes will continue to adjust closer to the convergent values until the higher energy fluxes reach steady state with the high-energy refilling timescale.

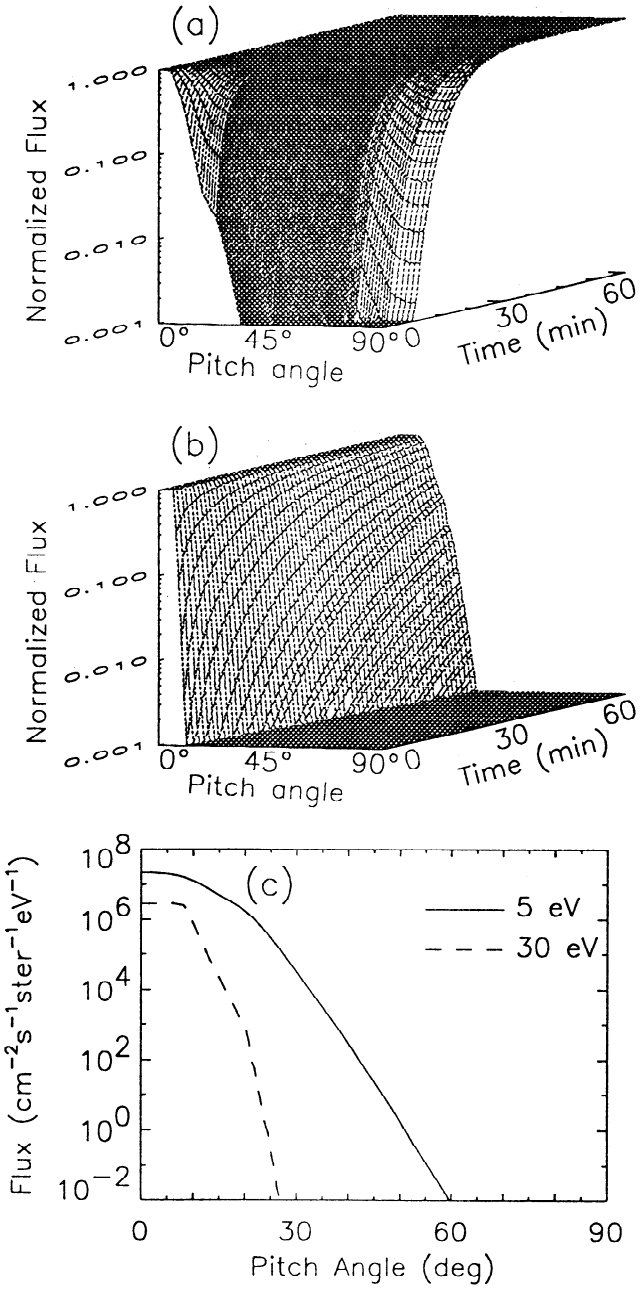

Figure 5. Equatorial pitch angle distributions for (a) 30 eV and (b) 5 eV for L=3 with an equatorial thermal plasma density of 17 cm^{-3}, with the (c) fluxes normalized to the steady state distribution at each pitch angle.

4. Plasmaspheric Transparency

One important aspect of the superthermal electron problem is their transport through the plasmasphere. The superthermal electrons escaping from the ionosphere experience small-angle scattering when traveling through the plasmasphere as a result of the Coulomb interaction with the thermal plasma. Because of this scattering, some of the superthermal electrons are scattered outside of the loss cone and undergo magnetic reflection: i.e., they become trapped. *Sanatani and Hanson* [1970] and *Nagy and Banks* [1970] presented qualitative discussions of electron trapping and the resulting increase in plasmaspheric heating, but the first attempts of quantitative calculations were those of *Gastman* [1973], *Takahashi* [1973], *Swartz et al.* [1975], *Lejeune and Worsmer* [1976] and *Khazanov et.al.* [1977].

By studying the ionosphere and plasmasphere as one system rather than two separate ones, substantial corrections are introduced in the values and characteristics of key parameters describing photoelectron fluxes [*Khazanov et al.*, 1994]. This is most clearly exemplified in the concept of the plasmaspheric transparency, which was introduced by *Takahashi* [1973] as the ratio of the number of particles leaving one end of a magnetic flux tube to the number of particles entering at the other end,

$$T(E)=\frac{\int_{\mu_{0B}}^{1}\mu_0\phi(E,\mu_0,s_1)d\mu_0}{\int_{\mu_{0B}}^{1}\mu_0\phi(E,\mu_0,-s_1)d\mu_0} \qquad (12)$$

where s_1 is the ionosphere-plasmasphere boundary altitude, taken to be 800 km in the present study. On the basis of the results of the "pure" plasmaspheric transport, it was shown that the transparency depends mainly on a single parameter proportional to the Coulomb cross section and to the total content of the thermal electrons in the magnetic force tube [*Takahashi*, 1973; *Lejeune and Worsmer*, 1976; *Krinberg and Matafonov*, 1978; *Khazanov et al.*, 1992]. The fact that processes are included such as diffusion across the loss cone boundary, reflection in the ionosphere due to elastic collisions with neutral and charged particles, and the redistribution of the flux at low energies due to interactions with neutral and charged particles, makes the term "transparency" acquire its conventional meaning (12) [*Khazanov et al.*, 1994].

Figure 6 shows the calculation of plasmaspheric transparency (12) based on the results of our new superthermal electron model. The transparency is presented as a function of energy for L=3 and L=4 for the different conditions of illumination, scattering processes in the conjugate hemispheres, and thermal plasma density descriptions along geomagnetic field line. Figures 6a and 6b show the transparencies which were obtained from steady state solutions of the coupled code using

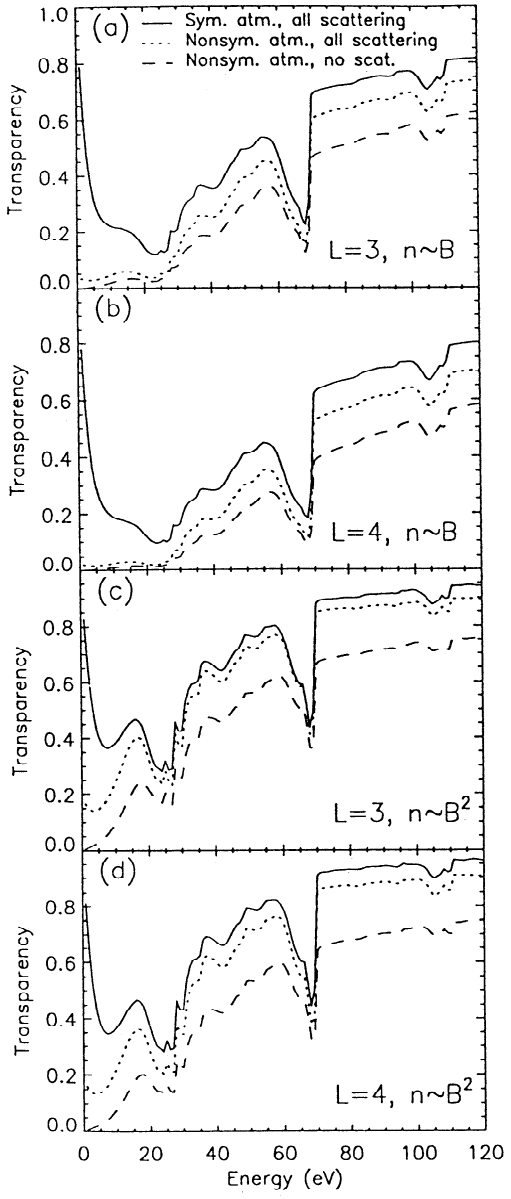

Figure 6. Plasmaspheric transparencies for (a) L=3 with $n_e \sim B$, (b) L=4 with $n_e \sim B$, (c) L=3 with $n_e \sim B^2$, and (d) L=4 with $n_e \sim B^2$.

plasmaspheric thermal density proportional to the magnetic field, and Figures 6c and 6d present the results for $n_e \sim B^2$. In each plot, the solid curve is the transparency for symmetric illumination with all scattering included for the entire field line, the dotted curve is for nonsymmetric illumination, and the dashed curve is for nonsymmetric illumination with scattering removed from the dark ionospheric region, so no particles escape from this ionosphere. The second and third transparencies are defined, for a given energy, as the number of electrons penetrating into the dark ionosphere divided by the number of electrons leaving the sunlit ionosphere.

As was mentioned before, "pure" plasmaspheric superthermal electron transport predicts the energy dependence of the plasmaspheric transparency to be primarily proportional to the Coulomb cross section and to the total content of the thermal electrons in the magnetic flux tube. In this case we should expect continuous increasing of plasmaspheric transparency from zero to one as energy increases. This does not reflect the results of the calculations presented in Figure 6, because they show considerable energy structure, and do not follow a simple increase with energy. These features are the result of the energy dependence of the superthermal electron flux created by photoionization and by collisional interactions between superthermal electrons and neutral particles in the ionosphere. As this flux propagates through the plasmasphere, particles undergo Coulomb collisions at a rate dependent on $\partial\phi/\partial E$ as seen from (2), and thus some structure is introduced into the transparency. The trough near 65 eV is due to the decrease in the photoelectron production spectrum at this energy. The increase of $T(E)$ with decreasing energy seen below $\approx$ 30 eV is caused by the formation of a plateaulike part of the photoelectron distribution function in the upper ionosphere and plasmasphere. The Coulomb collision term (2) is small in this situation because it contains the term $\partial\phi/\partial E$. The exact shape of the function at low energies, and therefore the location of the minimum in $T(E)$, depends on the total content of the thermal particles in the flux tube [*Khazanov et al.*, 1992]. Another effect which influences $T(E)$ at small energies is the trapped electron population, which diffuse down to low energies and subsequently into the loss cone, thereby increasing the value of the transparency. It is clear that in this case, $T(E)$ characterizes diffusion from the trapped region into the loss cone, rather than the transmitting capability of the flux tube [*Khazanov et al.*, 1994]. Notice the difference between Figures 6a and 6b with Figures 6c and 6d. When the total content in the flux tube is decreased (Figures 6c and 6d), the transparencies increase and more of the fine structure is evident. Features in the transparency become apparent when they are not damped by the thermal plasma, such as the formation at 15 eV and the two peaks at 25 and 30 eV.

There is also an L shell dependence in the transparency. Comparing Figure 6a with 6b and Figure 6c with 6d reveals that the higher L shells, with a larger amount of thermal plasma, have lower transparencies. To stress the dependence of the fine structure on ionospheric processes, plasmaspheric transparency (12) as a function of energy and L shell is shown in Figure 7, calculated with a version of the model that uses the continuous loss approximation [*Khazanov et al.*, 1994]. When this approximation is used, the fine structure almost disappears

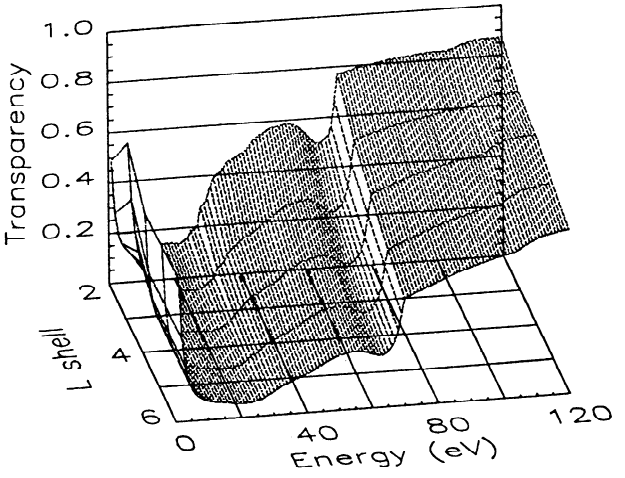

Figure 7. Plasmaspheric transparency for several L shells.

and the transparency is smoother than with the exact description of the loss processes. Notice that the 10-50 eV range contains only a trace of the structure evident in Figure 6, and the trough near 65 eV is not as pronounced. As with the previous figure, there is a gradual decrease in the transparency with increasing L shell corresponding to the increase in the total thermal content in the flux tube.

It is clear that plasmaspheric transparency is a complicated function. It depends not only on Coulomb collisions with the thermal plasma particles in the plasmasphere, but also on the primary photoelectron energy source, collisions with neutral and charged particles in the atmosphere and ionosphere, and diffusion across the loss cone boundary. Such dependencies, however, can be explained by the simple phenomenological model of plasmaspheric transparency derived by *Khazanov and Gefan* [1982] and *Khazanov et al.* [1994]. For the purposes of subsequent analysis, let us briefly present this phenomenological model, with some useful modifications introduced by *Gefan* [1985].

Let us introduce the following quantities: ε is the fraction of superthermal electron energy lost in the plasmasphere; β is the part of superthermal electron energy returned from the plasmasphere due to the electron scattering in the loss cone; $\alpha=1-\varepsilon-\beta$ is the "pure" part of plasmaspheric transparency; and A_1 and A_2 are the albedos of the ionosphere in the conjugate hemispheres. By taking into account multiple reflection in the ionosphere and plasmasphere the unidirectional fluxes P_1^+, P_2^+ at the boundaries of the ionosphere and plasmasphere (see Figure 8) can be presented in the form

$$P_1^+ = (P_{01}^+ + P_{02}^- \alpha A_1)\left[\left(1-\alpha^2 A_1 A_2\right)^{-1} + \beta A_1/(1-\beta A_1)\right] \quad (13)$$

$$P_2^- = (P_{02}^- + P_{02}^- \alpha A_2)\left[\left(1-\alpha^2 A_1 A_2\right)^{-1} + \beta A_2/(1-\beta A_2)\right] \quad (14)$$

$$P_2^+ = \alpha P_1^+ + \beta P_2^- \qquad P_1^- = \alpha P_2^- + \beta P_1^+ \quad (15)$$

Here P_{01}^+ and P_{02}^- are the fluxes entering the plasmasphere. These particles are generated in the ionosphere by photoionization or impact ionization.

Using (13)-(15) we can now derive an expression for the plasmaspheric transparency $T=P_2^+/P_1^+$ and consider the following cases:

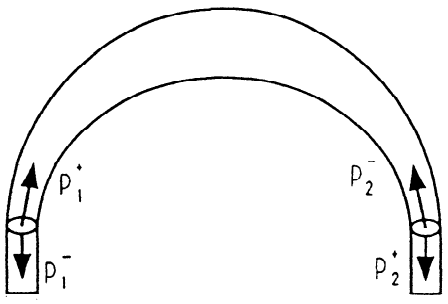

Figure 8. Flow schematic in a plasmaspheric flux tube.

Symmetrical conditions of illumination in the conjugate hemispheres ($P_{01}^+=P_{02}^-$ and $A_1=A_2=A$):

$$T_1 = \alpha+\beta \quad (16)$$

No source of superthermal electrons in region 2 ($P_{02}^-=0$):

$$T_2 = \alpha(1+\beta A) \quad (17)$$

No backscattering in the unilluminated ionosphere ($P_{02}^-=0$ and $A_2=0$):

$$T_3 = \alpha \quad (18)$$

Thus (16)-(18) show that the quantity $T(E)$ is not identical to the "pure" part of the plasmaspheric transparency α. Also, this phenomenological model explains the behavior of the transparency as a function of illumination and scattering processes in the conjugate hemispheres shown in Figure 6. T_1 corresponds to the solid curves where both ionospheres are sunlit and all scattering processes have been included. T_2 corresponds to the dotted curves, which have nonsymmetric conditions of illumination and include all of the scattering processes. T_3 pairs up with the dashed curves of nonsymmetric illumination with no scattering processes included in the dark ionosphere. It is clear that $T_1>T_2>T_3$ in all four situations presented in Figure 6, and from these transparencies the energy deposition processes of the plasmasphere can be examined.

5. Plasmaspheric Energy Interplay

Let us consider the superthermal electron energy redistribution in the plasmasphere system. This problem can be solved based on the calculation of the parameters $\alpha(E)$, $\beta(E)$, and $\varepsilon(E)$. The portion of particles traveling from one ionosphere to the conjugate ionosphere is described by the "pure" plasmaspheric transparency α; the part of superthermal electron energy reflected from the plasmasphere to the source ionosphere is β; and the fraction of energy lost in the plasmasphere is given by ε. To perform these calculations, we have used the values of $T(E)$, defined by (12), from our new model for the two different cases which correspond to (16) and (18) and are shown in Figure 6 as solid and dashed curves, respectively. Solving the system of two algebraic equations and using the relation $\alpha+\varepsilon+\beta = 1$ we find the unknowns α, β, and ε.

Figure 9 demonstrates the results of such calculations for L=3 and L=4 as a function of energy. Figure 9a is a plot of α, which was defined as the "pure" transparency, and represents the ability of a particle with a given energy to penetrate from one ionosphere through the plasmasphere into the conjugate ionosphere. The rise in α with energy is due to the decrease in the Coulomb cross section with energy. The formations of the fine structure in the 10-50 eV range are from photoelectron peaks that have undergone collisional changes through the plasmasphere, and the troughs at higher energies are also from structures in the photoelectron source that have been altered due to inelastic Coulomb collisions.

Particles that return to the initial ionosphere after being scattered in the plasmasphere are described by Figure 9b. Since the only plasmaspheric elastic scattering process included in the model is Coulomb scattering, β should, in general, have the same energy dependence as the Coulomb cross section. While the electrons are elastically scattering, they are also cascading in energy due to inelastic collisions, and this effect is seen in β

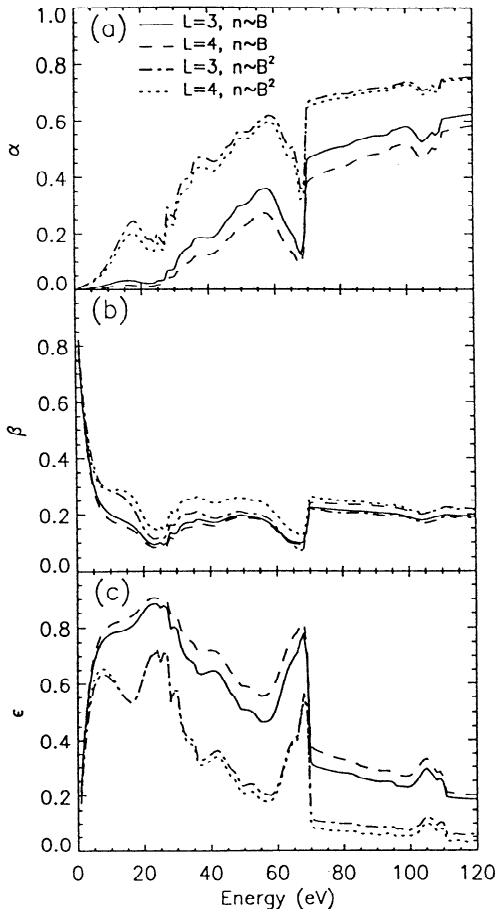

Figure 9. The plasmaspheric coefficients (a) α, (b) β, and (c) ε determined from the transparencies in Figure 6.

as an additional rise at low energies. Notice that there is a decrease in the 60-70 eV range, as in Figure 9a, and this is again due to the structure of the energy spectrum at that energy.

The quantity β can also be related to Figure 2. Notice in Figure 2a that the flux increases as the electrons approach the conjugate hemisphere. This feature is due to downward-flowing electrons backscattering into the upward-flowing stream. These reflected particles contribute to β because they are returned to their source ionosphere.

Figure 9c shows the fraction of energy deposited into the plasmasphere for each electron energy. The general shape of ε is a decrease with increasing energy because the Coulomb cross section is proportional to E^{-2}, but considerable structure is also present. This is because the efficiency of energy deposition is also proportional to $\partial\phi/\partial E$, and so the cascading of energy by the superthermal electrons is increased where there is a large decrease in flux over a short energy range. The energy lost by the superthermal electrons is transferred to the thermal plasma. This absorption is responsible for the peaks in the 60 - 70 eV and 100 - 110 eV ranges and also for the peaks below 50 eV. The decrease in ε below 20 eV is due to a decrease of the flux of low energy superthermal electrons caused by collisions with the thermal plasma. This decrease in the flux below 20 eV can also be seen in Figures 1 and 4.

The calculations presented in Figure 9 show the contribution of each energy to the plasmaspheric energy interplay. Integrating these three parameters from 1 to 150 eV, the energy range of the simulation, gives the portion of the total energy penetrating from the source ionosphere to the conjugate ionosphere, <α>; the part of the total energy reflected in the plasmasphere back to the source region, <β>; and the energy absorbed in the plasmasphere, <ε>. These values are given in Table 2.

As can be seen from these calculations, more of the energy from the source region is deposited into the conjugate ionosphere than back into the source ionosphere, that is, <α> is greater than <β> in every case. Also, the portion of the energy from the source region deposited to the plasmasphere is greater than the backscattered portion, that is, <ε> is greater than <β>. The relationship between <α> and <ε>, however, depends on the thermal plasma description and L shell. When $n_e \sim B$, about half of the energy is deposited into the plasmasphere while less than a third reaches the conjugate ionosphere for L=3 and L=4. When $n_e \sim B^2$, the percentages for <α> and <ε> reverse, so about half flows into the conjugate ionosphere while less than thirty percent is absorbed by the plasmaspheric thermal plasma. The relationship with L shell is less pronounced, and the change is usually 5% or less between L=3 and L=4.

Comparing the results of Table 2 and Figure 9 reveals energy ranges which contribute the most to each parameter. Figure 9a shows that energies above 50 eV are the largest contributors to <α>. It can be seen from Figure 9b that energies below 20 eV are the most likely to be reflected back to their source ionosphere. From Figure 9c it can be concluded that superthermal electrons with energies between 10 and 70 eV are the largest contributors of energy to the plasmaspheric thermal plasma.

It is worthwhile to compare <ε>, the portion of energy absorbed in the plasmasphere, with the calculations of *Newberry et al.* [1989]. In that study, a comparison was made between data from the retarding ion mass spectrometer (RIMS) on the Dynamics Explorer 1 (DE 1) satellite and the field line interhemispheric plasma (FLIP) model. The FLIP model included a phenomenological factor (trapping factor) to represent the amount of energy lost to the plasmasphere from the photoelectrons, and they concluded that good agreement is achieved between the calculated and measured ion temperatures when ~55 % of the total photoelectron flux is trapped in the plasmasphere. We conducted a similar study with our model and used the thermal electron profile in the ionosphere and plasmasphere from *Newberry et al.* [1989], and we found that <ε>=0.53. This shows that our calculations are in very good agreement with phenomenological modeling and measurements of the thermal structure of the plasmasphere.

6. Summary

Numerical solutions to the nonsteady state superthermal electron kinetic equation have been presented. The calcu-

Table 2. Plasmaspheric Energy Deposition Coefficients

	<α>	<β>	<ε>
L=3, $n_e \sim B$	0.316	0.192	0.491
L=4, $n_e \sim B$	0.265	0.195	0.540
L=3, $n_e \sim B^2$	0.504	0.206	0.290
L=4, $n_e \sim B^2$	0.483	0.243	0.274

lations were performed in the plasmasphere and the two conjugate ionospheres, self-consistently coupling the three regions. The model also includes various neutral particle ionization and excitation processes, scattering, and the effect of the inhomogeneous magnetic field. The distribution function in time, distance along arbitrary geomagnetic field lines, energy, and pitch angle are among the parameters calculated by the model. The results presented here show the complicated structure of the superthermal electron distribution, and this model is another step towards understanding the exchange of energy between spatial regions and particle populations in the ionosphere-plasmasphere system. The model can handle any magnetic field configuration, neutral atmosphere and thermal plasma description, and phase-space grid.

The superthermal electron flux distribution was shown in several ways and the features of these distributions were described in detail. Omnidirectional flux spectra and pitch angle distributions for given energies were presented for the steady state solution, while pitch angle distributions at specific altitudes and plasmaspheric omnidirectional flux spectra were used to display the nonsteady state results. The time needed to refill a depleted flux tube was found to be several elastic scattering timescales, which means that hours are required to reach the steady state flux levels for high energy superthermal electrons.

Plasmaspheric transparencies, $T(E)$, have been calculated for different conditions of illumination, scattering processes in the conjugate ionospheres, and descriptions of the thermal plasma density. It was found that $T(E)$ is a complicated function that depends not only on Coulomb collisions in the plasmasphere but also on the primary photoelectron energy spectrum, conditions of illumination, collisions with neutral and charged particles in the atmosphere and ionosphere, and diffusion across the loss cone boundary. A phenomenological description of plasmaspheric transparency was used to describe the energy interplay in the plasmasphere. By studying the ionosphere and plasmasphere as one system rather than two separate ones, substantial corrections are introduced in the values and characteristics of key parameters describing photoelectron fluxes.

The energy dependence and average values of the parameters α, β, and ε was discussed. The quantity α is the "pure" part of the transparency and describes particles traversing the plasmasphere from its source ionosphere to the conjugate ionosphere, β is the portion of superthermal electron energy reflected back to their source ionosphere, and ε is the energy lost to the plasmasphere. These parameters are dependent on energy, and the structure of each is related to the thermal plasma distribution and L shell. The electron energy ranges that contribute the most to each of these parameters were $E \geq 70$ eV for α, $E \leq 20$ eV for β, and 10 eV$<E<$70 eV for ε. Integrated values of these parameters were calculated and their importance in describing energy deposition was discussed. We also found that our calculations are in good agreement with the phenomenological theoretical study by *Newberry et al.* [1989], which is based on DE 1/RIMS data.

7. Future Development of the Model

There are several processes which will be incorporated into this model and discussed in upcoming publications. One development is coupling this model with a thermal plasma transport model. This will permit the calculation of the self-consistent electric field, which is generated when the highly mobile superthermal electrons stream into the plasmasphere ahead of the heavy ions and charge neutrality is violated. The inclusion of the self-consistent electric field allows for the proper coupling between the thermal and the superthermal plasmas. External electric fields, such as the electric field of magnetospheric convection, will also be incorporated.

Another effect which must be included at some time is the interaction with waves generated by an external source, such as ion-cyclotron waves from the ring current particles, plasmaspheric hiss, Alfven and magnetosonic waves, and electrostatic electron-cyclotron waves. There is some evidence that these waves can interact with the superthermal electrons; *Erlandson et al.* [1993] observed an enhancement in the superthermal electron fluxes in regions of increased wave activity by DE 2. If the energy density of the wave is large compared to the energy density of the superthermal electrons, the wave fields can be taken as constant functions in the term which describes the interaction with these waves. The inclusion of diffusion coefficients describing these waves would allow this model to describe these processes.

Plasma waves can also be amplified by instabilities in the superthermal electron distribution, and so a self-consistent feedback is needed to properly describe this process. As the distribution function becomes unstable, linear theory predicts that plasma waves will be amplified. These waves can then interact via diffusion terms and alter the superthermal electron distribution, and thus the amplification of the plasma waves will be changed. Incorporation of this self-consistent plasma wave interaction will also be conducted in the near future.

Acknowledgments. The authors would like to thank S. C. Solomon for kindly supplying the updated cross section data sets. They would also like to thank J. L. Horwitz, J. R. Jasperse, and T. E. Moore, for valuable discussions on this topic. This work was supported at the University of Michigan by the National Science Foundation under contract ATM-9412409.

The Editor thanks R. Link and another referee for their assistance in evaluating this paper.

References

Banks, P. M., and A. F. Nagy, Concerning the influence of elastic scattering upon photoelectron transport and escape, *J. Geophys. Res.*, *75*, 1902, 1970.

Banks, P. M., C. R. Chappell, and A. F. Nagy, A new model for the interaction of auroral electrons with the atmosphere: Spectral degradation, back scatter, optical emission and ionization., *J. Geophys. Res.*, *79*, 1459, 1974.

Bell, K. L., and R. P. Stafford, Photoionization cross sections for atomic oxygen, *Planet. Space Sci.*, *40*, 1419, 1992.

Bilitza, D., Progress report on IRI status, *Adv. Space Res.*, *10*,(11), 3, 1990.

Buonsanto, M. J., Comparison of incoherent scatter observations of electron density, and electron and ion temperature at Millstone Hill with the International Reference Ionosphere, *J. Atmos. Terr. Phys.*, *51*, 441, 1989.

Carpenter, D. L., and C. G. Park, On what ionospheric workers should know about the plasmapause-plasmasphere, *Rev. Geophys.*, *11*, 133, 1973.

Conway, R. R., Photoabsorption and photoionization cross sections: A compilation of recent measurements, *Memo Rep. 6155*, Nav. Res. Lab., Washington, D.C., 1988.

Corcuff, P., J. Corcuff, D. L. Carpenter, C. R. Chappell, J. Vigneron, and N. Kleimenova, La plasmasphère en période de recouvrement

magnétique. Etude combinée des données satellites OGO 4, OGO 5 et des sekfflements reçus au sol, *Ann. Geophys., 28*, 679, 1972.

Erlandson, R. E., T. L. Aggson, W. R. Hogey, and J. A. Slavin, Simultaneous observations of subauroral electron temperature enhancements and electromagnetic cyclotron waves, *Geophys. Res. Lett., 20*, 1723, 1993.

Fennelly, J. A., and D. G. Torr, Photoionization and photoabsorption cross sections of O, N_2, O_2, and N for aeronomic calculations, *At. Data Nucl. Data Tables, 51*, 321, 1992.

Gastman, I. J., Theoretical investigation and plasma line measurements of conjugate photoelectrons in the ionosphere, Ph.D. thesis, Univ. of Mich., Ann Arbor, 1973.

Gefan, G. D., The ionosphere-plasmasphere transport of suprathermal electrons, Ph.D. thesis, Irkutsk Univ., Irkutsk, Russia, 1985.

Gefan, G. D., A. A. Trukhan, and G. V. Khazanov, A method of calculating auroral electron fluxes, *Ann. Geophys.*, 3, 135, 1985.

Gefan, G. D., and G. V. Khazanov, Non-steady-state conditions of filling up the geomagnetic trap with superthermal electrons, *Ann. Geophys. 8*, 519, 1990.

Hedin, A.E., Extension of the MSIS thermospheric model into the midle and lower atmosphere, *J. Geophys. Res., 96*, 1159, 1991.

Hinteregger, H. E., Representations of solar EUV fluxes for aeronomical applications, *Adv. Space Res., 1*, 39, 1981.

Khazanov, G. V., *The kinetics of the electron plasma component of the upper atmosphere* (in Russian), Moscow, Nauka, 1979. (English translation, National Translation Center, #80-50707, Washington, D. C., 1980.)

Khazanov, G. V., and G. D. Gefan, The kinetics of ionosphere-plasmasphere transport of superthermal electrons, *Phys. Solariterr., 19*, 65, 1982.

Khazanov, G. V., M. A. Koen, and S. I. Baraishhuk, Trapped photoelectrons and secondary electrons in the midlatitude plasmasphere, I, II, *Cosmic Res., 15*, 68; 379, 1977.

Khazanov, G. V., M. A. Koen, Yu. V. Konikov, and I. M. Sidorov, Simulation of ionosphere-plasmasphere coupling taking into account ion inertia and temperature anisotropy, *Planet. Space Sci., 32*, 585, 1984.

Khazanov, G. V., T. I. Gombosi, A. F. Nagy, and M. A. Koen, Analysis of the ionosphere-plasmasphere transport of superthermal electrons,: 1., Transport in the plasmasphere, *J. Geophys. Res., 97*, 16,887, 1992.

Khazanov, G. V., M. W. Liemohn, T. I. Gombosi, and A. F. Nagy, Non-steady-state transport of superthermal electrons in the plasmasphere, *Geophys. Res. Lett., 20*, 2821, 1993a.

Khazanov, G. V., T. Neubert, G. D. Gefan, and A. A. Trukhan, E. V. Mishin, A kinetic description of electron beam ejection from spacecraft, *Geophys. Res. Lett., 20*, 1999, 1993b.

Khazanov, G. V., T. Neubert, and G. D. Gefan, Kinetic theory of ionosphere-plasmasphere transport of suprathermal electrons, *IEEE Trans. Plasma Sci., 22*, 187, 1994.

Kozyra, J. U., C. E. Valladares, H. C. Carlson, M. J. Buonsanto, and D. W. Slater, A theoretical study of seasonal and solar cycle variations of stable aurora red arcs, *J. Geophys. Res., 95*, 12219, 1990.

Krinberg, I. A., and G. K. Matafonov, Coulomb collision-induced photoelectron trapping by the geomagnetic field and electron gas heating in the plasmasphere, *Ann. Geophys., 34*, 89, 1978.

Lejeune, G., "Two stream" photoelectron distributions with interhemispheric coupling: A mixing of analytical and numerical methods, *Planet. Space Sci.*, 27, 561, 1979.

Lejeune, J., and F. Wormser, Diffusion of photoelectrons along a field line inside the plasmasphere, *J. Geophys. Res., 81*, 2900, 1976.

Link, R., Feautrier solution of the electron transport equation, *J. Geophys. Res.*, 97, 159, 1992.

Lummerzheim, D., M. N. Rees, and H. R. Anderson, Angular dependent transport of auroral electrons in the upper atmosphere, *Planet. Space Sci., 37*, 109, 1989.

Mantas, G. P., The theory of photoelectron thermalization and transport in the ionosphere, *Planet. Space Sci., 23*, 337, 1975.

Mantas, G. P., and J. C. G. Walker, The penetration of soft electrons into the ionosphere, *Planet. Space Sci., 24*, 409, 1976.

Nagy, A. F., and P. M. Banks, Photoelectron fluxes in the ionosphere, *J. Geophys. Res., 75*, 6260, 1970.

Newberry, I. T., R. H. Comfort, P. G. Richards, and C. R. Chappell, Thermal He+ in the plasmasphere: Comparison of observations with numerical calculations, *J. Geophys. Res., 94*, 15265, 1989.

Oran, E. S., and D. J. Strickland, Photoelectron flux in the Earth's ionosphere, *Planet. Space Sci., 26*, 1161, 1978.

Park, C. G., D. L. Carpenter, and D. B. Wiggin, Electron density in the plasmasphere: Whistler data on solar cycle, annual, and diurnal variations, *J. Geophys. Res., 83*, 3137, 1978.

Porter, H. S., F. Varosi, and H. G. Mayr, Iterative solution of the multistream electron transport equation, 1, Comparison with laboratory beam injection experiments, *J. Geophys. Res., 92*, 5933, 1987.

Prather, M. J., M. B. McElroy, and J. Rodriguez, Photoelectrons in the upper atmosphere: A formulation incorporating effects of transport, *Planet. Space Sci., 26*, 131, 1978.

Sanatani, S., and W. B. Hanson, Plasma temperature in the magnetosphere, *J. Geophys. Res., 75*, 769, 1970.

Solomon, S. C., P. B. Hays, and V. J. Abreu, The auroral 6300 Å emission: Observations and modeling, *J. Geophys. Res., 93*, 9867, 1988.

Stamnes, K., Analytic approach to auroral electron transport and energy degradation, *Planet. Space Sci., 28*, 427, 1980.

Strickland, D. J., D. L. Book, T. P. Coffey, and J. A. Fedder, Transport equation techniques for the deposition of auroral electrons, *J. Geophys. Res., 81*, 2755, 1976.

Swartz, W. E., G. J. Bailey, and R. J. Moffett, Electron heating resulting from interhemispherical transport of photoelectrons, *Planet. Space Sci., 23*, 589, 1975.

Takahashi, T., Energy degradation and transport of photoelectrons escaping from the upper ionosphere. *Rept. Ionos. Space Res. Jpn., 27*, (1), 79, 1973.

Torr, M. R., D. G. Torr, P. G. Richards, and S. P. Yung, Mid- and Low-latitude model of thermospheric emissions 1. $O^+(2P)$ 7320 Å and $N_2(2P)$ 3371 Å, *J. Geophys. Res., 95*, 21,147, 1990.

Victor, G. A., K. Kirby-Docken, and A. Dalgarno, Calculations of the equilibrium photoelectron flux in the thermosphere, *Planet. Space Sci.*, 24, 679, 1976.

G. V. Khazanov and M. W. Liemohn, Space Physics Research Laboratory, Department of Atmospheric, Oceanic, and Space Sciences, University of Michigan, Ann Arbor, MI 48109-2143.

(Received October 21, 1994; revised February 8, 1995; accepted February 8, 1995.)